CRYSTAL GROWTH & DESIGN

pubs.acs.org/crystal

Article

Pyknosil-to-Zeolite Hydrothermal Conversion of Magadiite into Mordenite

Rafael C. Lima, Felipe F. Barbosa, Carla Peron, Gustavo Chacón-Rosales, Joaquín Martínez-Ortigosa, Tiago P. Braga, Christian W. Lopes,* and Sibele B. C. Pergher*

Cite This: *Cryst. Growth Des.* 2026, 26, 1100−1112

Read Online

ACCESS | Metrics & More | Article Recommendations | Supporting Information

ABSTRACT: Layered silicates can be versatile precursors for the preparation of porous materials. Their transformation into zeolites typically employs organic structure-directing agents and seed-assisted crystallization, as in interzeolite conversions. Several zeolite topologies have been synthesized using magadiite; however, the role of magadiite in these processes remains unclear. The recent resolution of the magadiite structure provides an opportunity to integrate and reinterpret existing knowledge on this topic. Here, we report an unusual conversion of the layered hydrous silicate magadiite into mordenite triggered solely by the external addition of aluminum to a precrystallized magadiite gel. Aluminum disperses in the solid, occupying distinct framework sites, while a reorganization of ring-building units occurs, resulting in a marked decrease in the amount of surface silanol/silanolate groups. This restructuring proceeds without evidence of amorphization, accompanied by a progressive increase in surface area and growth of morphologically prismatic mordenite particles in contact with the magadiite plate-like particles. This transformation of a dense pyknosil-like structure into an open zeolite framework exhibits features of solid-phase reorganization triggered by aluminum supplied from the solution. These findings introduce a seed- and OSDA-free route for converting layered silicates into zeolites, expanding the conceptual and synthetic space for tailored microporous materials.

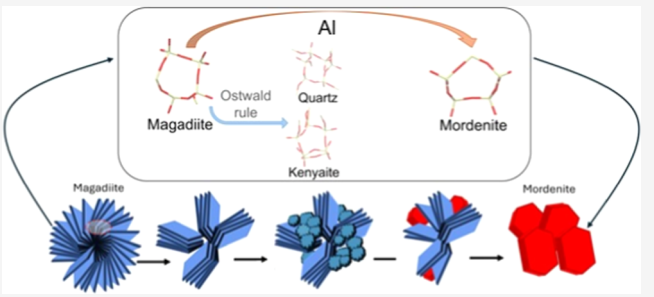

1. INTRODUCTION

With their distinct layered structures and reactive surfaces, two-dimensional solids provide versatile platforms for applications in electronics, catalysis, and adsorption. Their tunable architectures also enable the development of alternative synthesis routes and the design of novel functional materials.[1] Layered hydrous silicates are composed exclusively of silicon tetrahedral layers terminated by silanol and silanolate groups, whose nucleophilic oxygens facilitate structural modification.[2]

Magadiite is a hydrous layered silicate synthesized via established hydrothermal methods.[3] It has been applied in drug delivery,[4,5] CO_2 capture,[6] dye removal,[7] and catalysis.[8] Its surface silanol groups allow for functionalization and structural modification, including exfoliation, pillaring, and metal incorporation.[6,9−12] Several studies have shown that aluminum can be incorporated into the magadiite framework through hydrothermal treatment without the formation of other phases.[12−15]

The transformation of layered silicates into porous crystalline frameworks offers valuable opportunities for tuning structure and function. Among these materials, zeolites are particularly prominent due to their well-established properties. Several zeolite topologies[16−24] have been synthesized using magadiite as a component of the synthesis gel. These studies focused on the effectiveness of zeolitization, leaving the role of the silicate framework in these transformations unclear. However, the determination of the crystal structure of magadiite[25] provides an opportunity to integrate and reinterpret existing knowledge on this topic, enabling an investigation of whether such processes involve true solid−solid conversion, partial dissolution, or complete recrystallization.

Several aspects of the zeolitization of amorphous and crystalline phases have been discussed, focusing on mechanisms that involve either solution-mediated species transport or diffusionless solid-state transformations.[26−31] Typical metastable phase formation routes, such as conventional hydrothermal synthesis, are classified as solution-mediated processes that involve dynamic mass transport between the solution and solid phases.[31] The presence of a crystalline phase in the synthesis gel can promote the nucleation of new crystals that retain structural motifs from the parent phase.[32,33]

Received: August 10, 2025
Revised: December 27, 2025
Accepted: December 29, 2025
Published: January 19, 2026

https://doi.org/10.1021/acs.cgd.5c01166
Cryst. Growth Des. 2026, 26, 1100−1112

Structure-directing agents are often employed to support the process. Most reported hydrothermal zeolite interconversions are interpreted using this model. Nevertheless, some studies have suggested an alternative, in which the solid phase undergoes reconstruction through a pathway dependent on the structural similarity between the two phases.[29,34]

In this context, we investigate the transformation of magadiite into zeolite mordenite without the use of seeds or structure-directing agents. Unlike typical zeolite-to-zeolite interconversions, which tend to follow Ostwald's rule, this process involves a transition from the dense pyknosil-like layers of magadiite to a more open zeolite framework. Moreover, most reported conversions of nonzeolitic silicates to zeolites[35−37] also involve aluminum already present in the precursor structure. In contrast, magadiite is a pure silica layered solid. Thus, the conversion requires the external addition of aluminum to promote the transition to mordenite, representing an uncommon pathway with respect to conventional zeolitization methods.

The unusual combination of features applied to this study resulted in an unconventional transformation route with potential implications for silicate chemistry. The process was monitored at multiple stages by analyzing structural changes, aluminum coordination and dispersion, acidity, surface properties, and morphology. Particular attention was given to the evolution of structural order to assess whether the process occurs via a continuous framework reconstruction or through a dissolution−reprecipitation pathway. This study adds new insights into the processes governing silicate-to-zeolite transformations and highlights an alternative approach for zeolite synthesis.

2. EXPERIMENTAL SECTION

2.1. Synthesis Procedure

The materials were obtained by hydrothermal treatment. The gel with molar composition 3 SiO_2: NaOH: Na_2CO_3: 46 H_2O was prepared by mixing the required amount of fumed silica Aerosil 200 (Degussa) with an aqueous alkaline solution containing sodium hydroxide (Sigma-Aldrich, >98%) and anhydrous sodium carbonate (Dinâmica Química, 99.5%). The mixture was agitated for 15 min. The gel was placed in a Teflon-lined stainless-steel autoclave, sealed, and subjected to hydrothermal treatment at 150 °C. After 48 h of hydrothermal treatment, the autoclave was slightly cooled and opened to add aluminum triisopropylate (ATiP) (Merck, 98%) in an amount to achieve a Si/Al ratio of 10. In additional experiments, ATiP was replaced by sodium aluminate (Riedel de-Haen, 56% Al_2O_3, 45% Na_2O) to evaluate the effect of the aluminum source (detailed description in SI). The Al-containing gel was mixed for a few minutes, sealed, and then subjected to hydrothermal treatment for periods from 1.5 to 24 h. The products after this period were labeled "2d + Xh," where "X" represents the time (h) after the addition of the Al source. A diagram (Scheme S1) summarizes all the synthesis procedures. The collected samples were filtered, washed with water until the filtrate reached pH 7, and dried at 60 °C.

The NH_4^+-form of the samples was obtained by cationic exchange with a 0.1 mol·L^{-1} NH_4Cl solution (1 g/100 mL ratio). The suspension was kept under agitation at room temperature for 24 h and then filtered. This process was repeated twice. The samples were filtered and washed with distilled water until no chloride was detected. The samples were then dried at 60 °C for 16 h. The H-form of samples was obtained by calcination of NH_4^+-form samples in air at 450 °C for 3 h (heating rate of 3 °C·min^{-1}).

2.2. Characterization

Crystalline structure data were evaluated by powder X-ray diffraction on a Bruker D2 Phaser X-ray diffractometer using CuKα radiation with a Ni filter, which operated at a 10 mA current and 30 kV voltage with a sample holder rotation of 15 rpm. The analysis was performed with a divergent slit of 0.6 mm and anti-scatter screen of 1.0 mm. The scanning was performed stepwise, with 0.01° increments and an accumulation time of 0.1 s. The lower and upper discrimination values were 0.11 and 0.25 V, respectively. The signal collection was performed with a LYNXEYETM detector (192 channels).

^{27}Al MAS NMR spectra measurements, $\nu_0(^{27}Al)$ = 78.2 MHz, were carried out on a Bruker Avance III 300 spectrometer in a 4 mm probe spinning the sample at 10 kHz, with a $\pi/2$ excitation pulse width of 0.5 μs and 5s as a recycle delay. ^{29}Si MAS NMR spectra, $\nu_0(^{29}Si)$ = 79.5 MHz, were recorded on a Bruker Avance III HD 400 MHz spectrometer with a 7 mm probe spinning the sample at 5 kHz, using a ^{29}Si pulse length of 4.0 μs and 180 s as a recycle delay. The ^{27}Al and ^{29}Si NMR spectra were referenced to $Al(NO_3)_3$ and TMS, respectively. To calculate the Si/Al ratio, eq 1 was applied.[38]

$$\frac{Si}{Al} = \frac{\sum_{n=0}^{4} I_{Si(nAl)}}{\sum_{n=0}^{4} \frac{nI_{Si(nAl)}}{4}} \quad (1)$$

Fourier-transform medium-infrared spectroscopy (FTIR) analysis was conducted on a Shimadzu IRAffinity-1 spectrometer over the spectral region of 400−4000 cm^{-1} with a resolution of 4 cm^{-1} using the KBr pellet technique. Near-infrared spectra were collected using an Agilent Cary 5000 spectrometer. Raman spectra were collected using a Horiba LabRam Evolution spectrometer with a 532 nm excitation wavelength.

Textural properties were studied by N_2 physisorption at 77 K using Micromeritics ASAP 2020. The textural properties were calculated according to the IUPAC recommendations.[39] The specific surface area (S_{BET}) was obtained from the BET method,[40] micropore volume ($V_{\mu P}$), and external area (S_{ext}) were calculated from the α_s-plot method[41] with macroporous silica LiChrospher Si-1000 as the reference material,[42] and the total pore volume (V_{TP}) was calculated using the Gurvich rule at 0.985 of relative pressure.[43]

Acidity was evaluated by ammonia temperature-programmed desorption (NH_3-TPD). The data were obtained using a multipurpose testing unit with an online quadrupole mass detector, QUADSTAR 422 (QMS 200, BALZERS). Approximately 100 mg of the sample was treated under a flow of He (60 mL·min^{-1}) for 1 h at 450 °C. Then, the sample was cooled to 100 °C and saturated with NH_3/He (4 vol %) for 1 h; the physisorbed NH_3 was removed by He flow (60 mL·min^{-1}) for 1 h at the same temperature. Finally, the sample was heated until 800 °C (20 °C·min^{-1}) under He flow (60 mL·min^{-1}), and the NH_3 desorption was monitored using a thermal conductivity detector (TCD). The nature of the acidity was indirectly observed by testing the samples in the glycerol dehydration reaction. The tests were conducted at atmospheric pressure and 250 °C using N_2 as the carrier gas for 5 h. Typically, 0.2 g of H-form sample was placed in a borosilicate reactor and pretreated at 350 °C under an N_2 atmosphere (30 mL·min^{-1}) for 30 min. A 10 wt % glycerol solution was introduced into the reactor using a syringe pump at a flow rate of 3.6 mL·h^{-1} combined with N_2 (30 mL·min^{-1}) as the carrier gas. Aliquots were collected every hour using a trap containing a mixture of water/ice and salt for GC analysis. The catalytic reaction data were analyzed using a PerkinElmer Clarus 680 gas chromatograph using a polar cast silica column (5% diphenyl/95% dimethylsiloxane). Glycerol conversion was calculated through eq 2, and product selectivity was determined according to eq 3.

$$C_{glycerol} = \frac{\text{amount of consumed glycerol}_{mol}}{\text{amount introduced in the reactor}_{mol}} \times 100\% \quad (2)$$

$$S_{product} = \frac{\text{amount of product obtained}_{mol}}{\text{amount of consumed glycerol}_{mol}} \times 100\% \quad (3)$$

Morphology was examined using a Zeiss Auriga 40 field emission scanning electron microscope. Energy dispersive spectroscopy (SEM-EDS) maps were obtained in a Tescan Vega 4 scanning electron

https://doi.org/10.1021/acs.cgd.5c01166
Cryst. Growth Des. 2026, 26, 1100−1112

microscope. HAADF-STEM-EDS maps were collected in a JEOL 2100F at 200 kV. Inductively coupled plasma emission spectroscopy (ICP-OES) was used to analyze the Si, Al, and Na content. The sample was digested by adding HF(aq) (40%), HCl(aq) (30%), and HNO_3(aq) (65%) diluted in ultrapure water. The device used was a Varian 715-ES-ICP-Optical Emission Spectrometer, and CHN elemental analysis was performed on Eurovector EuroEA3000 using sulfanilamide as a reference.

3. RESULTS AND DISCUSSION

XRD patterns (Figure 1) depict the crystallization of magadiite and its phase transition to mordenite. After 48 h of hydrothermal treatment (Figure 1a), all reflections corresponding to the magadiite phase, particularly at 5.7° 2θ, associated with the basal d-spacing, are observed, indicating a well-crystallized phase. Operational yields are listed in Table S1.

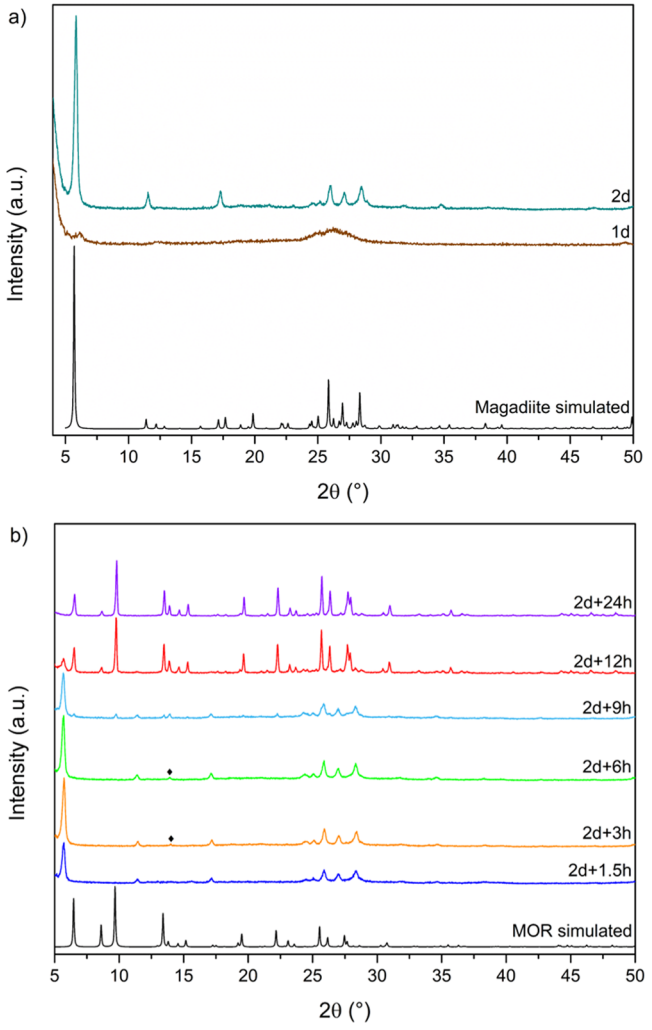

Figure 1. X-ray diffraction patterns showing the phase transition from magadiite to mordenite: (a) before adding aluminum and (b) after adding aluminum. After 48 h, all the characteristic peaks of the magadiite phase are present. After adding aluminum, a peak close to the one assigned to the (130) reflection in the MOR phase appears in the 2d + 3h sample. No amorphous silica halo is evident after magadiite crystallization. After 24 h, all the peaks are due to the MOR phase.

The sample collected immediately before the ATiP addition (2d) (Figure 1b) shows only the magadiite pattern. A new low-intensity reflection appears at ∼14° 2θ in 2d + 3h (see Figure S1), absent from the magadiite reference pattern. It lies near the MOR (130) reflection at 13.8°, which intersects the chains of four- and five-membered rings. In conventional MOR syntheses, reflections in other regions often emerge before (130).[44,45] In the 2d + 6h sample, this peak shifts toward the MOR pattern position at 13.8°.

At the stage of the 2d + 9h sample, most characteristic diffraction peaks of the MOR phase are detectable, although with low relative intensity, and all magadiite reflections are present. In the 2d + 12h sample, reflections of magadiite are no longer evident, apart from that one around ∼6° 2θ, indicating that the two-dimensional structure persists at this stage alongside the complete set of mordenite peaks. The conversion is completed in the 2d + 24h sample, which presents only MOR phase peaks.

No amorphous halo or crystalline phases other than magadiite and mordenite are evident within the resolution of the techniques used in this work, differing from other time-resolved zeolite conversions in which additional transient phases or amorphous intermediates have been detected.[46−49] Similar behavior was reported in an in situ diffraction study for LTA-to-ABW interzeolite conversion, promoted by a lithium chloride solution.[28] The authors described the process as epitaxial crystallization on the surface of the solid phase, driven by building units shared between the topologies. It was also concluded that no significant amorphous phase was detected as the crystallization progressed within the resolution of time-resolved XRD.

In the absence of aluminum, magadiite is kinetically persistent in its synthesis medium. Prolonged hydrothermal treatment of a conventional magadiite gel for several days after its formation leads to its conversion into the denser layered silicate kenyaite or cristobalite/quartz.[50−52] The addition of aluminum alters the pathway of metastable phases, leading to an atypical conversion. The rapid appearance of the MOR phase can be attributed to the sharing of similar building units with the magadiite phase. Interzeolite conversions have been explained based on the sharing of building units and cross-nucleation.[53−55] The 5-membered rings in both phases (Figure S2), as ring-building units (RBU) nanoparts, may act as drivers of the process.[56] As observed from crystallographic information files (CIF), in magadiite, these rings are exposed on surfaces oriented toward the interlayer region and intersected by multiples of the (001) plane.[57] In orthorhombic mordenite, they are intersected by the (130) plane on lateral prism faces, which is in the same region as the first nonmagadiite peak in XRD patterns (Figure S3). This correspondence agrees with the domain matching between the phases.

The dynamics between aluminum and the interlayer space of magadiite also influence the process. The intercalation rate of organic cations into magadiite is faster than the crystallization processes,[23] making it reasonable to assume that the same applies to aluminum aquacomplexes. Since the interlayer space is the only accessible region in magadiite,[25] aluminum is transported there. Theoretical predictions indicate that aluminum can occupy octahedral positions in the surface groups and tetrahedral positions within the twisted rings of the framework.[58] Under alkaline conditions, the olation and oxolation reactions occur, either incorporating Al into the silicate layers or making it into a center of framework reorganization.

https://doi.org/10.1021/acs.cgd.5c01166
Cryst. Growth Des. 2026, 26, 1100−1112

The presence of aluminum is known to influence the relative stability of silicate bonds. Theoretical calculations indicate that the formation of Si−O−Al bonds requires less energy than Si−O−Si bonds,[59] which supports the view that aluminum incorporation into the silicate framework may be more favorable than pathways leading to denser pure-silica phases when aluminum is added. Moreover, under the same conditions used in this work, mordenite zeolite does not form from a conventional gel containing amorphous silica under the investigated conditions, suggesting that the role of magadiite in the conversion extends beyond the behavior expected for a typical silica source.[44]

Additional syntheses were conducted to assess whether magadiite plays a role beyond serving as a silica source. In one experiment, the gel composition was identical to the original synthesis. In another, fumed silica was entirely replaced by previously synthesized magadiite. In both cases, ATiP was added immediately after gel preparation, and the gels were treated for 24 h under the same post-ATiP conditions as in the original synthesis. The resulting XRD patterns (Figure S4) confirmed that, in the absence of magadiite, mordenite does not form under the same conditions.

Another set of complementary syntheses was conducted to evaluate the possible role of isopropyl as an organic structure-directing agent (Figure S5). One synthesis followed the original procedure, except that sodium aluminate was added after 48 h instead of ATiP. The other used a gel identical to the original, but sodium aluminate was added immediately after preparation instead of ATiP. The results confirm that when starting from fumed silica, mordenite is not formed after 24 h. The excess sodium and the Al species produced by sodium aluminate, which differ from those generated by ATiP,[60,61] can promote direct zeolite crystallization but require adjustments in synthesis parameters to yield a well-crystallized product. These results demonstrate that the conversion does not depend on isopropyl as an OSDA. CHN elemental analysis of the 2d + 24h sample (Table S2) shows no organic residues within micropores, corroborating that the isopropyl species do not contribute to the phase transition, being released into the solution.

The solid-state ^{27}Al MAS NMR spectra (Figure 2a) show the evolution of the aluminum coordination environments in the preformed structures. The ^{27}Al MAS NMR spectra of the sample collected immediately after aluminum addition (2d + 0h) and the 2d + 1.5h sample exhibit two broad signals. The signal at δ ^{27}Al ≈ 60 ppm indicates aluminum in tetrahedral coordination, whereas the signal at δ ^{27}Al ≈ 10 ppm corresponds to octahedral coordination.[62] This chemical shift differs from that associated with extra-framework species in crystalline aluminosilicates.[38] It may be due to the non-dissolved aluminum source and aluminum species confined within the interlayer space, resembling the environments in Al_2O_3.[63]

The Al(IV) signal increases, while the Al(VI) signal concomitantly decreases from the 2d + 3h to 2d + 9h samples. The Al(IV) signal becomes asymmetric, with its maximum shifting downfield at δ ^{27}Al ≈ 64 ppm, consistent with the spectrum reported for Al-containing magadiite.[15] In partially disrupted zeolite frameworks, line-shape asymmetry is often attributed to perturbed framework Al sites, typically revealed by a shoulder near 40 ppm.[64,65] Here, the asymmetry of the signal is centered at a higher chemical shift, indicating Al(IV) in a more distorted environment than in the zeolite

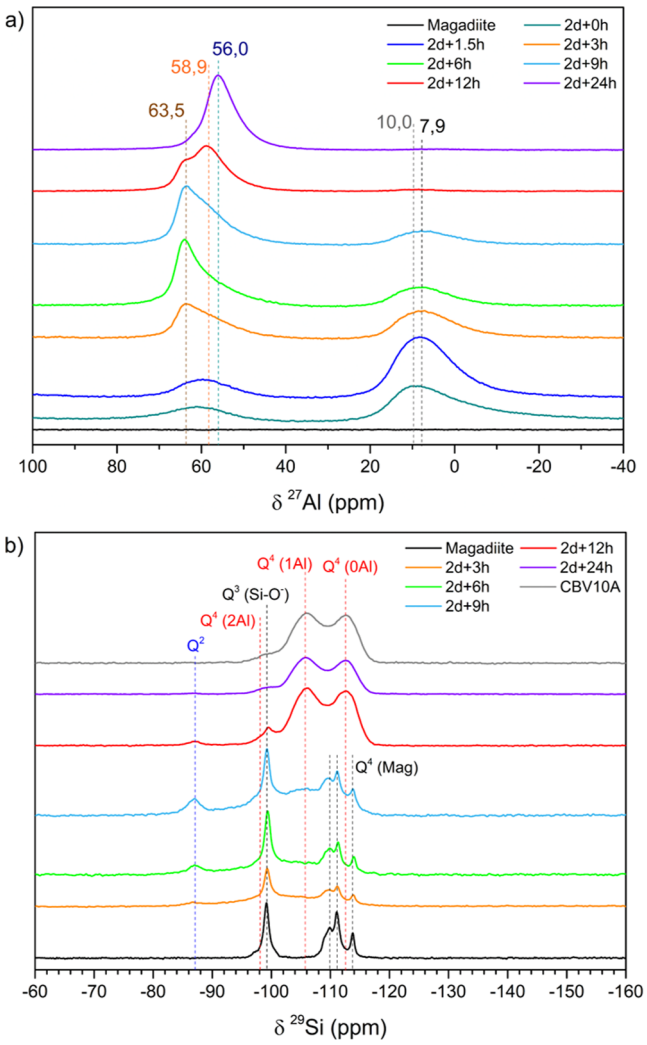

Figure 2. Solid-state MAS NMR spectra: (a) ^{27}Al and (b) ^{29}Si. The aluminum coordination environment evolves throughout the conversion due to changes in the silicate framework.

frameworks.[66] The signal shape also suggests the coexistence of multiple Al(IV) environments, as shown in the deconvolution (Figure S6).

Moreover, in the sample 2d + 9h, the high-field part of the Al(IV), around δ ^{27}Al ≈ 56 ppm, the typical region where the Al(IV) appears in mordenite,[67] becomes more prominent, correlating with the appearance of additional XRD peaks of MOR.

The ^{27}Al MAS NMR spectrum of the 2d + 12h sample mainly consists of a combination of signals related to Al(IV) containing three components (Figure S6): Al(IV) in the magadiite phase (63.9 ppm), in the MOR phase (55.8 ppm), and the most intense signal, resulting from Al being converted from the MAG to the MOR environment at 59.4 ppm. This third chemical environment at 55.8 ppm lies near the expected range for mordenite and may reflect less distorted Al(IV) sites in the developing mordenite phase. A small Al(VI) signal due to species external or in the interlayer space is also present.

The spectrum of the 2d + 24h sample consists of a unique signal of tetrahedral Al at 56 ppm (deconvoluted into two components, see Figure S6) in the mordenite phase.[68]

In summary, the ^{27}Al MAS NMR results suggest an alumina-like contribution at early times (samples 2d and 2d + 1.5h). As

https://doi.org/10.1021/acs.cgd.5c01166
Cryst. Growth Des. 2026, 26, 1100−1112

the synthesis proceeds (samples 2d + 3h and 2d + 6h), the Al(IV) signal appears with a broad, asymmetric line shape and a chemical shift near ∼64.2 ppm, consistent with distorted tetrahedral environments. At longer times (2d + 9h, 2d + 12h, and 2d + 24h), the Al(IV) signal displays a more symmetric line shape, around ∼56 ppm, consistent with the coordination observed in mordenite (MOR). This progression in line shape and chemical shift supports that aluminum occupies tetrahedral sites in magadiite and evolves into the chemical environment of the mordenite framework.

Previous studies suggest that Al incorporation can stabilize silicate frameworks against dissolution[69] and the split-synthesis approach[70] suggests that, once aluminum is incorporated into a silicate framework, its stability increases.

In the ^{29}Si MAS NMR spectra (Figure 2b), up to the 2d + 6h sample, the spectra primarily exhibit the typical narrow signals of magadiite. The signals at −109 to −114 ppm are characteristic of hydrous layered silicates and result from a splitting of the Q^4 signal, corresponding to $[Si(OSi)_4]$ units.[8,71,72] The most intense signal, at −99.2 ppm, is attributed to the Q^3 signal, representing both $[Si(OSi)OH]$ and $[Si(OSi)O^-]$ groups located on the surface of the layers.[71,73] This signal decreases in intensity during the phase transition, indicating the occurrence of condensation reactions in the interlayer space, promoting a change in the environment from silanol/silanolate groups to Q^4 units. Also, there is a signal at −87.0 ppm, assigned to Q^2 sites in magadiite,[14] where Q^2 and Q^3 species typically appear as a broad, overlapping contribution.[74,75]

In the 2d + 9h sample, variations appear in the −103 and −106 ppm region. Signals in this range have been assigned to Q^4(1Al) units.[76−78] The gradual increase of this signal is indicative of the reconstruction of the framework involving aluminum-incorporated units. By 2d + 12h sample, this region consolidates a signal at −105.8 ppm, consistent with Q^4 signals observed in some zeolites, including mordenite.[79] At the same time, the signals at −87.0 and −99.2 ppm broaden and decrease in intensity due to the emergence of a resonance at −98.1 ppm, assigned to Q^4(2Al) units of the MOR phase. This decrease is consistent with the condensation of the hydroxyl groups from the magadiite.

The spectrum of the 2d + 24h sample displays the three characteristic signals of mordenite zeolite.[79] Signals at −98.1, −105.8, and −112.5 ppm correspond to Q^4(2Al), Q^4(1Al), and Q^4(0Al), respectively. Applying eq 1 to calculate the framework Si/Al ratio, the 2d + 12h and 2d + 24h samples resulted in 6.2 and 6.0, respectively. The Si/Al ratio and the spectrum of the 2d + 24h sample are similar to those of commercial mordenite CBV10A, which has a comparable Si/Al ratio. This demonstrates an increase in aluminum in the framework over time.

On the other hand, ICP analysis (Table 1) shows that the bulk ratios vary only modestly throughout the conversion. Compared with NMR results, elemental analysis is consistent with aluminum interacting with magadiite, followed by its incorporation into the MOR framework.

SEM-EDS maps (Figure S7) show that, up to the 2d + 9h sample, Al is initially concentrated in large aggregates. As zeolite formation proceeds, aluminum distribution becomes progressively more uniform within the particles. STEM-EDS maps of representative samples (2d + 3h, 2d + 9h, and 2d + 24h) (Figure S8) indicate that, in the 2d + 3h sample, Al was not detected under our STEM-EDS conditions over the lamellar regions. Afterward, in the 2d + 9h sample, Al appears as heterogeneous hotspots colocalized with the plate-like particles. Finally, in the 2d + 24h sample, Al is dispersed within the prismatic particles.

Table 1. Elemental Content by ICP-OES Analysis

sample	Si (%)	Al (%)	Na (%)	Si/Al	Na/Al
MAG	38.7	-	5.4	-	-
2d + 3h	32.5	5.7	5.6	5.7	1.0
2d + 6h	32.9	6.4	6.6	5.1	1.0
2d + 9h	33.5	6.9	7.6	4.9	0.9
2d + 12h	34.0	6.8	5.8	5.0	1.2
2d + 24h	34.4	6.4	5.1	5.3	1.2

The NH_3-TPD results (Table 2 and Figure S9) show a trend of increasing acidity as the transition phase develops.

Table 2. Acidity Evolution of the Samples Determined by NH_3-TPD

sample	LT (%)	HT (%)	total (μmol·g^{-1})
MAG	-	100	21
2d + 3h	-	100	12
2d + 9h	-	100	38
2d + 12h	18	82	835
2d + 24h	28	72	2697

According to prior findings,[80] pure magadiite should not exhibit detectable acid sites by spectroscopic or thermal methods. However, the analyzed sample displays slight acidity. Up to the 2d + 9h sample, acidity remains nearly unchanged, despite the growth of the MOR phase, likely because structural reorganization renders the acid sites inaccessible. A marked increase in acidity is observed in the 2d + 12h sample, consistent with the predominance of the MOR phase.

The acidity varies across the full range of strengths throughout the conversion. Magadiite and the 2d + 3h sample show peaks similar to those reported for pure silica and Al-containing magadiite,[13] likely arising from silanol/silanolate groups and the initial interaction with the aluminum species in the interlayer space.

In the 2d + 9h sample, a peak broadening is observed toward the region of medium acidity, possibly reflecting structural rearrangement. The 2d + 12h and 2d + 24h samples display the characteristic profile of mordenite.[81]

Glycerol dehydration products are directly influenced by the acidic nature of the catalyst, thereby serving as a probe to characterize changes in acid sites during the phase transition, as previously reported for other model reactions.[82] Acrolein formation is associated with Brønsted acid sites, whereas acetol production is linked to Lewis acid sites.[83] In all samples, acrolein is the major product, indicating the prominence of Brønsted acidity. The selectivity for acrolein increases (Figure 3) in parallel with the growth of the MOR phase.

The chromatogram (Figure S10) confirms that glycerol remains unconverted in the absence of a catalyst. When pure magadiite is used, a reaction occurs in the interlayer space, resulting in poor selectivity (Figure S11). As in silica gel, silanol behaves as Brønsted acid sites, whereas silanolate behaves as Lewis acid sites.[84]

The slight increase in conversion for the 2d + 3h sample may stem from the small amount of incorporated aluminum, as deprotonated Si−O−Al sites have higher proton affinity than

https://doi.org/10.1021/acs.cgd.5c01166
Cryst. Growth Des. 2026, 26, 1100−1112

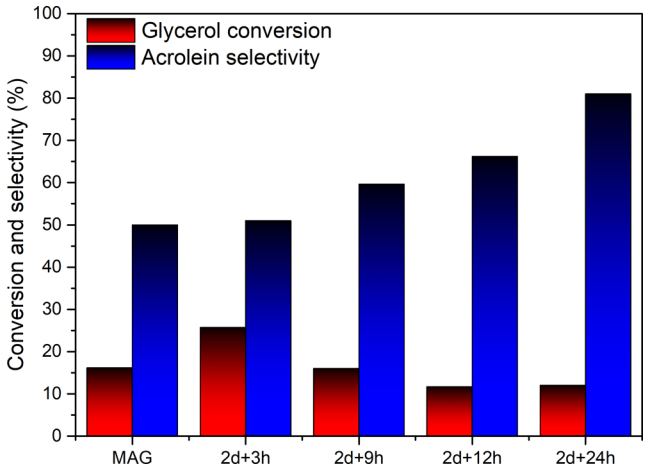

Figure 3. Glycerol conversion and acrolein selectivity of the samples tested in the glycerol dehydration. The selectivity for acrolein increases with the incorporation of aluminum. The conversion decreases with the zeolite framework growth.

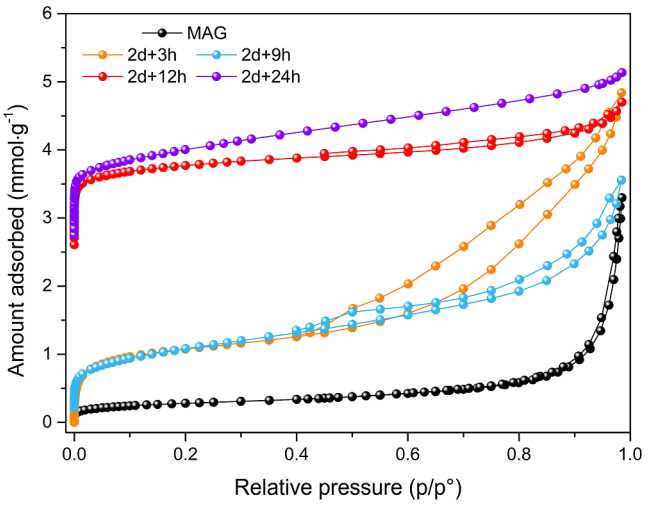

Figure 4. N_2 sorption isotherms of magadiite and synthesized samples. The magadiite isotherm presents a layered non-porous solid profile. Between 3 and 9 h, the constancy in N_2 adsorption at low pressures, combined with the decrease at high pressures, suggests that the external surface diminishes, while the specific surface area remains almost constant.

silanolates.[85,86] In the 2d + 9h sample, acrolein selectivity rises due to micropore formation from the developing MOR phase and the associated increase in surface area, as observed for a set of aluminosilicates with similar Si/Al ratios and total acidity.[87] In parallel, part of the silanol groups shifts from germinal and vicinal terminal types to the more acidic internal "nest" type, contributing to the increase in acidity with the emerging Al(IV) sites.[88−90]

Overall conversion decreases because glycerol access is hindered by the pseudo-one-dimensional pore architecture of MOR, leading to rapid pore blockage, typical of 1D-channel zeolites, even for smaller molecules.[64,91,92] The byproducts, mainly acetol and acetaldehyde, show a decreasing trend in selectivity. This behavior may be related to the reduced availability of silanolate/silanol surface groups as condensation and zeolite formation progress.

From 2d + 9h, the selectivity trends mirror the changes indicated by NH_3-TPD. The 2d + 12h sample shows a modest rise in byproduct formation, likely because residual magadiite silanolates and nonincorporated aluminum shift to act as Lewis acid sites once Brønsted sites are deactivated. The 2d + 24h sample attains the highest acrolein selectivity, in agreement with the complete development of the MOR phase and stabilization of Brønsted acidity.

The N_2 adsorption/desorption isotherms (Figure 4) show that the isotherm of the MAG sample (corresponding to pure Na-magadiite) is type II, typical of nonporous solids, and gradually transitions into a type I(b) isotherm, characteristic of zeolites presenting interparticle porosity.

The 2d + 3h sample isotherm indicates the emergence of micropore filling at low relative pressures, consistent with an incipient formation of a porous phase. Between the 2d + 3h and 2d + 9h samples, the overall uptake at intermediate pressures decreases, and the hysteresis loop changes from type H3, typical of slit-like voids between stacked plates, to type H4, associated with narrow slit-like porosity.[39] This suggests a progressive reduction of the layered domains toward microporous zeolite.

Conversely, the microporous surface area, observed at small relative pressures, remains essentially unchanged, pointing to a transient stage of external reorganization. This behavior contrasts with that observed in dissolution-recrystallization-based zeolite interconversions in which stepwise syntheses at different reaction times consistently reveal structural degradation during the transformation.[46,48,49,93,94]

From 2d + 9h to 2d + 12h, a sharp rise in low-pressure uptake is consistent with the development of framework microporosity. The hysteresis contracts into a narrower and nearly linear loop, while the external surface area decreases. This combination suggests that a limited number of narrow slit-like voids remain interconnected.

Finally, in the 2d + 24h sample, the slight increase in the adsorption at low relative pressures suggests that microporosity is essentially developed in the 2d + 12h sample. The hysteresis is no longer observed, reflecting the loss of interconnectivity among interparticle voids at this stage.

The textural properties (Table 3) show that the specific surface area increases slightly 3 h after aluminum addition and remains constant between the 2d + 3h and 2d + 9h samples, while the external surface area decreases. After this interval, the specific surface area increases. Relating this observation to the XRD data, the increase in specific surface area and micropore volume coincides with the appearance of the new peak at 3 h. The data may suggest a stage in which the zeolite phase development is preceded by reorganization among the particles.

Table 3. Textural Properties of a Typical Magadiite and Some Samples of This Study[a]

sample	S_{BET} ($m^2 \cdot g^{-1}$)	$V_{\mu P}$ ($cm^3 \cdot g^{-1}$)[a]	S_{ext} ($m^2 \cdot g^{-1}$)[b]	V_{TP} ($cm^3 \cdot g^{-1}$)[c]
MAG	20	0	20	0.09
2d + 3h	90	0.03	90	0.16
2d + 9h	90	0.01	70	0.12
2d + 12h	340	0.11	50	0.16
2d + 24h	350	0.11	74	0.18

[a]Volume of micropores. [b]External and secondary pore surface. [c]Volume of total pores.

https://doi.org/10.1021/acs.cgd.5c01166
Cryst. Growth Des. 2026, 26, 1100−1112

From the 2d + 12h sample, the specific surface area increases further, consistent with the predominance of mordenite phase, as observed in XRD data. The further increase in external surface area in the 2d + 24h sample suggests that particles expose external interfaces that provide additional accessible surface.

From FTIR spectra (Figure 5), the band at 3662 cm^{-1} is assigned to the stretching vibrations of isolated surface OH

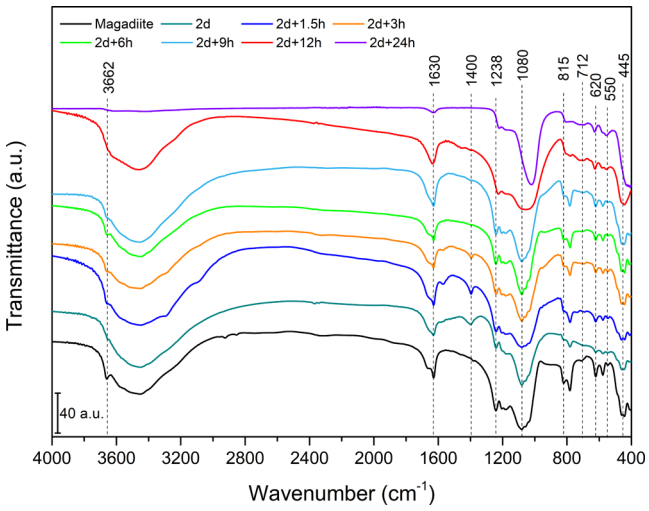

Figure 5. Mid-FTIR spectra of a typical magadiite and the synthesized samples.

groups that are not involved in hydrogen bonding[95] and gradually disappears as the MOR phase increases, indicating the occurrence of condensation reactions. The doublet at 1600 cm^{-1}, attributed to bending vibrations of the water, results from the correlation splitting of A_1 symmetry-related species[95] and merges into one band as the MOR phase grows.

The band around 1400 cm^{-1}, observed only in the early stages of the transition, and absent in both pure phases[95−97] can be correlated with transitional bonds. In the last stages, small shifts to lower frequencies in the asymmetric stretching mode of TO_4 units at 1080 cm^{-1} can be attributed to framework aluminum incorporation, as reported for zeolites with different Si/Al ratios.[98] Four shoulders near the main band, all assigned to the same vibration, progressively merge into a single feature at 1230 cm^{-1}, ascribed to the internal stretching of MOR D5R units,[99] which also shifts, indicating incorporation of aluminum into these rings.

The bands around 815 cm^{-1}, 777 cm^{-1}, and 712 cm^{-1} are associated with the symmetric stretching vibration of T−O bonds in both phases. The region around 600−500 cm^{-1} is sensitive to structure[100] and associated with D5R units in zeolites, but without assignment for magadiite.[57]

The hydroxyl region was examined through near-infrared spectroscopy (Figure S12a). The range at 7500−6800 cm^{-1} corresponds to the first overtone ($\nu O \rightarrow 2OH$) of the hydroxyl vibrations on the surface and water involved in hydrogen bonds.[101] The shoulder at 6840 cm^{-1} is related to strong hydrogen bonds[102] and lacks definition as the conversion occurs (Figure S12b). The band at 5250 cm^{-1} is due to vibrations of H_2O and shifts to a lower wavenumber. The region around 4500 cm^{-1} presents bands attributed to interactions of terminal groups and structural bonds.[103] It can be observed that the band profile tends to disappear with the MOR phase. These changes can be associated with the condensation of silanolate groups, which interact strongly with other hydroxyl groups and cations.

According to the Raman spectra (Figure 6), the band at 1060 cm^{-1} is attributed to the interaction of silanolate groups

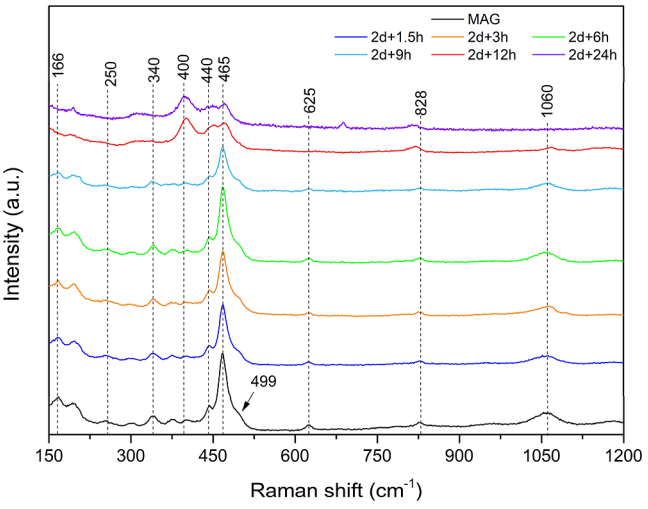

Figure 6. Raman spectra of the obtained samples. The changes in the bands between 500 and 220 cm^{-1} highlight the transformation of ring-building units throughout the layered silicate-to-zeolite conversion.

with the interlayer space in magadiite[95,104] and to the asymmetrical stretching of T−O−T bonds in mordenite.[97] The band at 830 cm^{-1} is associated with the symmetrical stretching of T−O−T bonds and shifts as the conversion progresses, as occurs in FTIR. The range between 700 and 400 cm^{-1} is associated with symmetrical stretching vibrations. Some of these bands are sensitive to changes in bond angles,[95] such as the one at 625 cm^{-1} that decreases with the increase of the MOR phase.

The band at 465 cm^{-1} is attributed to the symmetric stretching of four-membered rings in zeolites containing five-membered rings.[105,106] A similar assignment can be extended to the magadiite structure since it comprises complex rings. The bands at 499 cm^{-1} and 440 cm^{-1} are associated with the torsional mode of silanolate groups. The intensity of these bands decreases with the growth of the MOR phase, which aligns with the reduction in ring strain and siloxane groups as the framework reorganizes.[106]

The bands below 400 cm^{-1} have not been fully identified.[95] However, they are related to charge compensation cations and hydration.[104] The band at 400 cm^{-1} is attributed to the bending of five-membered rings of MOR, increasing in the last stages of the conversion.[105] The bands at 350−225 cm^{-1}, assigned to six and seven-membered rings in zeolites, disappear as the MOR phase increases.[107] The band at 250 cm^{-1} can be related to the pseudoeight-membered ring in magadiite, such as a band in the same region attributed to eight-membered rings in mordenite, which is not observable in Vis-Raman.[105] The bands below 225 cm^{-1} are related to the host species and decrease with the siloxanes.[104,106]

Morphological changes observed in SEM images (Figures 7 and S13) indicate that the addition of aluminum causes the magadiite particles to lose their cauliflower-shaped arrangement (Figure S14), without significantly altering the structural

https://doi.org/10.1021/acs.cgd.5c01166
Cryst. Growth Des. 2026, 26, 1100−1112

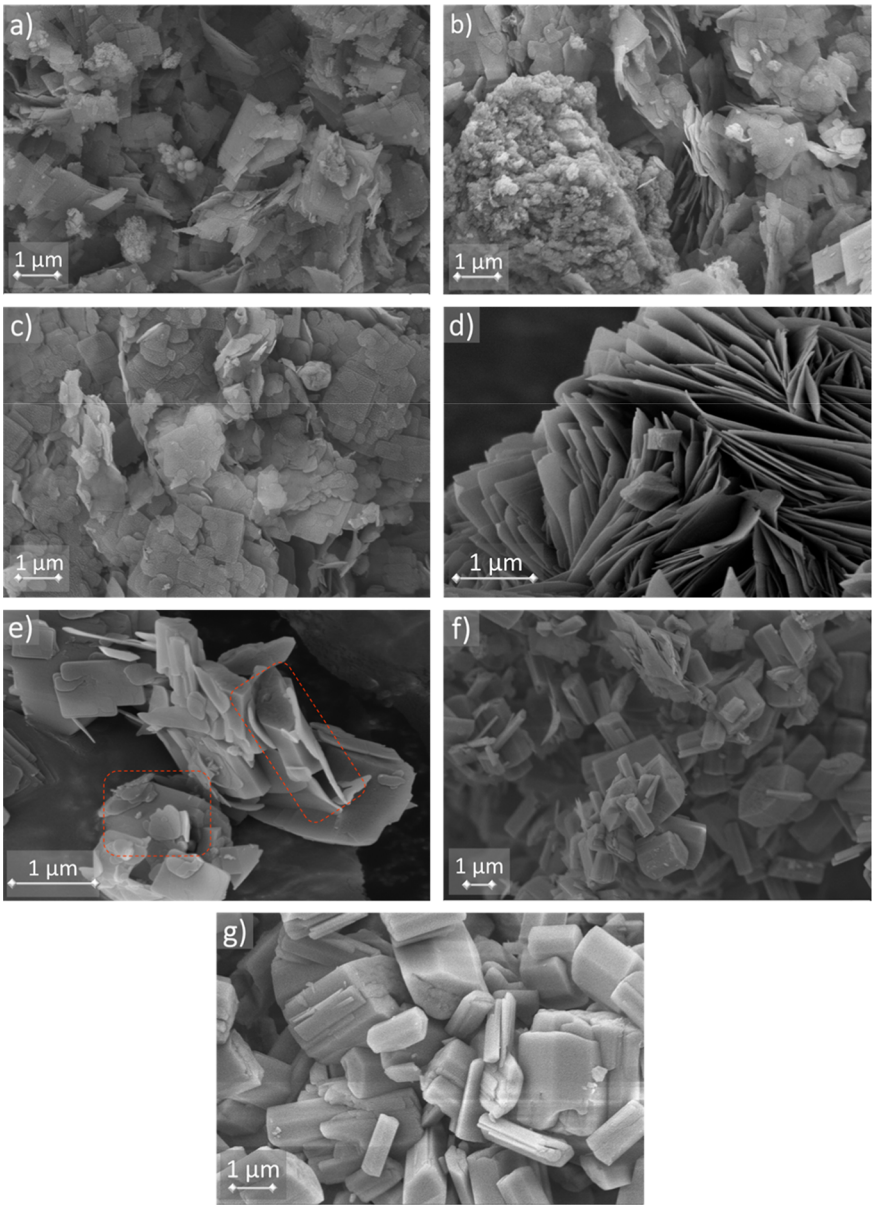

Figure 7. SEM images of the samples obtained: (a) 2d + 0h, (b) 2d + 1.5h, (c) 2d + 3h, (d) 2d + 6h, (e) 2d + 9h, (f) 2d + 12h, and (g) 2d + 24h. The partially disordered plate-like particles decrease in size, while the three-dimensional particles grow between them. The red squares highlight the prismatic particles among the plate-like particles.

stacking of the layers. The other morphology that appears immediately after ATiP is added to the gel (2d + 0h sample) is likely associated with the ATiP-derived species.

The 2d + 6h sample shows a few small prismatic particles among plate-like particles. These prisms become larger with time, while the plate-like particles gradually decrease in size, as seen in the SEM images of the 2d + 9h and 2d + 12h samples. In mordenite, the *c* direction coincides with the 12-membered channel axis and defines the hexagonal end faces,[53] and the lateral prism faces are parallel to the (130) plane. Accordingly, prism-plate contact is observed predominantly along the lateral faces.

Subsequently, most of the particles exhibit the typical mordenite habit. By the 2d + 24h sample, all plate-like particles are consumed. The worm-like morphology of amorphous aluminosilicate precursors[108−110] was not observed in any sample.

The magadiite framework is composed of small, highly twisted rings in a pyknosil-like structure denser than any known pure-silica zeolite structure.[25,57,111] Mordenite is a large-pore zeolite of open structure. A pyknosil-to-zeolite structure conversion is unusual compared to other conversions to zeolites, in which the initial phase appears to participate with large structural motifs such as building units. This transformation also diverges from Ostwald's Rule, which is frequently invoked to rationalize transformations from less packed to denser phases based on the relative stability of silicate bonds.[26,32] Nevertheless, precedents exist in which more compact frameworks transform into more open ones,[26,112] the structural contrast here is more pronounced than in zeolite−zeolite interconversions.

Partial dissolution of the parent phase is observed in magadiite conversions to zeolites in the presence of SDAs or seeds[21,113,114] and zeolite interconversions.[48,49] However, the

https://doi.org/10.1021/acs.cgd.5c01166
Cryst. Growth Des. 2026, 26, 1100−1112

analyses did not show evidence of magadiite dissolution. Aluminum is absent from the parent phase and thus acts as the sole element linking two kinetically persistent silicate phases under conditions that would otherwise drive magadiite toward denser products. Moreover, the synthesis proceeds without seeds, conventional structure-directing agents, or identical structural motifs that would enable a transition involving condensation of silanols.

Accordingly, this magadiite-to-MOR hydrothermal conversion route represents a particular case of zeolite synthesis. The data are consistent with a process involving framework reconstruction[27,29] promoted by aluminum supplied from the solution, akin to that proposed for ilerite-to-zeolite conversions, but without lattice continuity that could be associated with topotactic processes.[34]

4. CONCLUSIONS

This study reveals an unusual pathway for the direct conversion of magadiite into mordenite, driven by the incorporation of aluminum. Spectroscopic data indicate that aluminum follows a path from the precursor, passing through the solution to the interlayer space of magadiite. Once there, it gradually disperses in the solid by migrating through different crystallographic sites during framework incorporation. During this process, a transformation of ring-building units occurs, accompanied by a decrease in silicate surface groups.

NH_3-TPD measurements corroborate this scenario, revealing a progressive increase in acidity consistent with condensation of surface groups and the formation of framework-confined Brønsted sites. Catalytic data, used as a probe reaction, mirror this progression, showing that acrolein selectivity increases as byproduct formation decreases in step with the decline of Lewis acid sites from silanolate and nonincorporated aluminum.

Textural analysis shows a gradual development of microporosity, distinct from that seen in interzeolite conversions. The stage of external surface reorganization, without the retraction of the specific surface area observed in transformations between zeolites, aligns with the restructuring of the solid phase. Morphological observations corroborate this surface rearrangement, indicating the growth of prismatic particles in contact with the faces of the plate-like crystals.

This conversion exhibits features drawn from current zeolitization models. The shared ring motifs, cross-nucleation, and bond dissociation/formation energetics enable aluminum to trigger a progressive reorganization of the layered lattice toward the MOR topology without evidence of prior amorphization of the parent phase. While it shares traits with zeolite interconversion and solid-phase reorganization mediated by aluminum supplied by the solution, it also suggests that compositional control can override Ostwald's rule, inhibiting the direct crystallization of denser frameworks.

Overall, this work contributes to the understanding of zeolite synthesis by documenting a pyknosil-like-to-zeolite phase transition promoted solely by the external addition of aluminum into a preformed layered hydrous silicate. Beyond its mechanistic significance, this system provides an opportunity to observe a process similar to interzeolite conversion, but with a structural element external to the original gel composition, rather than by seed-driven synthesis. These findings expand the conceptual landscape of zeolite synthesis and may aid in the design of tailored microporous materials.

■ ASSOCIATED CONTENT

Supporting Information

The Supporting Information is available free of charge at https://pubs.acs.org/doi/10.1021/acs.cgd.5c01166.

Additional information, XRD patterns, CHN elemental analysis, deconvoluted ^{27}Al-NMR data, NH_3-TPD data, EDS maps, Infrared spectra, chromatogram, and additional SEM image (PDF)

■ AUTHOR INFORMATION

Corresponding Authors

Christian W. Lopes − *Laboratório de Catálise e Caracterização de Materiais. Departamento de Química, Universidade Federal do Paraná (UFPR), Curitiba, Paraná 81531-980, Brazil;* orcid.org/0000-0001-8420-1958; Email: christianwittee@ufpr.br

Sibele B. C. Pergher − *Laboratório de Peneiras Moleculares. Instituto de Química, Universidade Federal do Rio Grande do Norte (UFRN), Natal 59078-900, Brazil;* Email: sibelepergher@gmail.com

Authors

Rafael C. Lima − *Laboratório de Peneiras Moleculares. Instituto de Química, Universidade Federal do Rio Grande do Norte (UFRN), Natal 59078-900, Brazil;* orcid.org/0000-0002-4202-3345

Felipe F. Barbosa − *Laboratório de Peneiras Moleculares. Instituto de Química, Universidade Federal do Rio Grande do Norte (UFRN), Natal 59078-900, Brazil*

Carla Peron − *Instituto de Tecnología Química (ITQ), Consejo Superior de Investigaciones Científicas-Universitat Politècnica de València, 46022 Valencia, Spain*

Gustavo Chacón-Rosales − *Instituto de Tecnología Química (ITQ), Consejo Superior de Investigaciones Científicas-Universitat Politècnica de València, 46022 Valencia, Spain;* orcid.org/0000-0001-5280-608X

Joaquín Martínez-Ortigosa − *Instituto de Tecnología Química (ITQ), Consejo Superior de Investigaciones Científicas-Universitat Politècnica de València, 46022 Valencia, Spain; Laboratorio de Nanotecnología Molecular, Departamento de Química Inorgánica, Universidad de Alicante, Alicante 03690, Spain;* orcid.org/0000-0003-0468-676X

Tiago P. Braga − *Laboratório de Peneiras Moleculares. Instituto de Química, Universidade Federal do Rio Grande do Norte (UFRN), Natal 59078-900, Brazil*

Complete contact information is available at: https://pubs.acs.org/10.1021/acs.cgd.5c01166

Author Contributions

R.C.L.: investigation, methodology, visualization, formal analysis, writing—original draft, review, and editing. F.F.B.: investigation, formal analysis, and writing—original draft. C.P.: formal analysis. G.C.-R.: formal analysis. J.M.-O.: writing, formal analysis, and review. T.P.B.: review and editing. C.W.L.: conceptualization, visualization, supervision, formal analysis, review, and editing. S.B.C.P.: conceptualization, supervision, and review.

https://doi.org/10.1021/acs.cgd.5c01166
Cryst. Growth Des. 2026, 26, 1100−1112

Funding

The Article Processing Charge for the publication of this research was funded by the Coordenacao de Aperfeicoamento de Pessoal de Nivel Superior (CAPES), Brazil (ROR identifier: 00x0ma614).

Notes

The authors declare no competing financial interest.

■ ACKNOWLEDGMENTS

R.C.L. acknowledges Coordenação de Aperfeiçoamento de Pessoal de Nível Superior (CAPES) for the PhD scholarship. J.M.O. acknowledges the financial support from the European Union—NextGeneration EU through the Universitat Politècnica de València, Ministerio de Universidades, Plan de Recuperación, Transformación y Resiliencia for the Margarita Salas grant. NUCAT-UFRJ is acknowledged for the NH_3-TPD measurements. C.P. and C.W.L. acknowledge Conselho Nacional de Desenvolvimento Científico e Tecnológico—CNPq for the financial support.

■ REFERENCES

(1) Čejka, J.; Morris, R. E.; Nachtigall, P.; Roth, W. J. Layered Inorganic Solids. *Dalton Trans.* **2014**, *43* (27), 10274−10275.
(2) Ramos, F. S. O.; Munsignatti, E. C. O.; Pastore, H. O. 2D-3D Structures: The Hydrothermal Transformation of a Layered Sodium Silicate, Na-RUB-18, into Mordenite Zeolite. *Microporous Mesoporous Mater.* **2013**, *177*, 143−150.
(3) Dietzel, M.; Letofsky-Papst, I. Stability of Magadiite between 20 and 100°C. *Clays Clay Miner.* **2002**, *50* (5), 657−666.
(4) França, D. B.; Torres, S. M.; Filho, E. C. S.; Fonseca, M. G.; Jaber, M. Understanding the Interactions between Ranitidine and Magadiite: Influence of the Interlayer Cation. *Chemosphere* **2019**, *222*, 980−990.
(5) Ge, M.; Tang, W.; Du, M.; Liang, G.; Hu, G.; Jahangir Alam, S. M. Research on 5-Fluorouracil as a Drug Carrier Materials with Its in Vitro Release Properties on Organic Modified Magadiite. *Eur. J. Pharm. Sci.* **2019**, *130* (September 2018), 44−53.
(6) Vieira, R. B.; Pastore, H. O. Soft-Pillared@Magadiite: Influence of the Interlayer Space and Amine Type on CO2 Adsorption. *Dalton Trans.* **2018**, *47* (9), 3102−3111.
(7) Mokhtar, M. Application of Synthetic Layered Sodium Silicate Magadiite Nanosheets for Environmental Remediation of Methylene Blue Dye in Water. *Materials* **2017**, *10* (7), 760.
(8) Supronowicz, W.; Roessner, F.; Schwieger, W.; Meilikhov, M.; Esken, D. Synthesis and Properties of Sn-Containing Magadiite. *Clays Clay Miner.* **2012**, *60* (3), 254−264.
(9) Atulba, S. L. S.; Jang, J. H.; Park, M. TiO2-Pillared Magadiite and Its Arsenic Adsorption Capacity. *J. Porous Mater.* **2019**, *26* (1), 311−318.
(10) Park, K. W.; Jung, J. H.; Seo, H. J.; Kwon, O. Y. Mesoporous Silica-Pillared Kenyaite and Magadiite as Catalytic Support for Partial Oxidation of Methane. *Microporous Mesoporous Mater.* **2009**, *121* (1−3), 219−225.
(11) Katabathini, N.; El, M.; I. H. A; Mokhtar, M. Cu, Fe and Mn Oxides Intercalated SiO2 Pillared Magadiite and Ilerite Catalysts for NO Decomposition. *Appl. Catal., A* **2021**, *616* (March), 118100.
(12) Moura, H. M.; Pastore, H. O. Functionalized Mesoporous Solids Based on Magadiite and [Al]-Magadiite. *Dalton Trans.* **2014**, *43* (27), 10471−10483.
(13) Almeida, R. K. S.; Paz, G. L.; Báfero, G. B.; Pastore, H. O. Properties of Layered [Al]- and [V,Al]-Magadiite Catalysts as Revealed by Ethanol Dehydration. *Microporous Mesoporous Mater.* **2019**, *284* (March), 1−9.
(14) Moura, H. M.; Bonk, F. A.; Vinhas, R. C. G.; Landers, R.; Pastore, H. O. Aluminium-Magadiite: From Crystallization Studies to a Multifunctional Material. *CrystEngComm* **2011**, *13* (17), 5428−5438.
(15) Superti, G. B.; Oliveira, E. C.; Pastore, H. O.; Bordo, A.; Bisio, C.; Marchese, L. Aluminum Magadiite: An Acid Solid Layered Material. *Chem. Mater.* **2007**, *19* (17), 4300−4315.
(16) Pál-Borbély, G.; Beyer, H. K.; Kiyozumi, Y.; Mizukami, F. Recrystallization of Magadiite Varieties Isomorphically Substituted with Aluminum to MFI and MEL Zeolites. *Microporous Mater.* **1997**, *11* (1−2), 45−51.
(17) Feng, F.; Balkus, K. J. Recrystallization of Layered Silicates to Silicalite-1. *Microporous Mesoporous Mater.* **2004**, *69* (1−2), 85−96.
(18) Wang, Y.; Shang, Y.; Wu, J.; Zhu, J.; Yang, Y.; Meng, C. Recrystallization of Magadiite into Offretite in the Presence of Tetramethylammonium Cations. *J. Chem. Technol. Biotechnol.* **2010**, *85* (2), 279−282.
(19) Lv, T.; Wang, Y.; Zhang, S.; Feng, Z.; Zheng, J.; Yang, J.; Liu, X.; Liu, X.; Meng, C. Conversion of Magadiite to Pure-Silica-Nu-1 and an Insight into the Changes in Its Medium-Range Structure during Crystallization. *Inorg. Chem. Front.* **2019**, *6* (3), 837−847.
(20) Zhang, S.; Hu, J.; Wang, Y.; Lv, T.; Qu, X.; Zhang, H.; Meng, C. Organic Template-Free Synthesis of CHA Zeolite by Hydrothermal Conversion of Magadiite with the Assistance of Seeds and an Investigation of Crystallization Mechanism. *Microporous Mesoporous Mater.* **2024**, *380*, 113297.
(21) Wang, Y.; Lv, T.; Ma, Y.; Tian, F.; Shi, L.; Liu, X.; Meng, C. Synthesis and Characterization of Zeolite L Prepared from Hydrothermal Conversion of Magadiite. *Microporous Mesoporous Mater.* **2016**, *228*, 86−93.
(22) Zhang, S.; Lv, T.; Feng, Z.; Wang, F.; Liu, X.; Wang, W.; Wang, Y.; Meng, C. OSDA-Free Synthesis of Zeolite Beta by Magadiite Hydrothermal Conversion Method and an Insight into the Changes of Medium-Range Structure during Crystallization. *Microporous Mesoporous Mater.* **2019**, *278* (November 2018), 81−90.
(23) Selvam, T.; Schwieger, W. Synthesis and Characterization of Mordenite (MOR) Zeolite Derived from a Layered Silicate, Na-Magadiite. *Stud. Surf. Sci. Catal.* **2002**, *142 A*, 407−414.
(24) Shi, Z.; Wang, Y.; Meng, C.; Liu, X. Hydrothermal Conversion of Magadiite into Mordenite in the Presence of Cyclohexylamine. *Microporous Mesoporous Mater.* **2013**, *176*, 155−161.
(25) Krysiak, Y.; Maslyk, M.; Silva, B. N.; Plana-Ruiz, S.; Moura, H. M.; Munsignatti, E. O.; Vaiss, V. S.; Kolb, U.; Tremel, W.; Palatinus, L.; Leitão, A. A.; Marler, B.; Pastore, H. O. The Elusive Structure of Magadiite, Solved by 3D Electron Diffraction and Model Building. *Chem. Mater.* **2021**, *33* (9), 3207−3219.
(26) Maldonado, M.; Oleksiak, M. D.; Chinta, S.; Rimer, J. D. Controlling Crystal Polymorphism in Organic-Free Synthesis of Na-Zeolites. *J. Am. Chem. Soc.* **2013**, *135* (7), 2641−2652.
(27) Devos, J.; Shah, M. A.; Dusselier, M. On the Key Role of Aluminium and Other Heteroatoms during Interzeolite Conversion Synthesis. *RSC Adv.* **2021**, *11* (42), 26188−26210.
(28) Norby, P. Hydrothermal Conversion of Zeolites: An *in Situ* Synchrotron X-Ray Powder Diffraction Study. *J. Am. Chem. Soc.* **1997**, *119* (22), 5215−5221.
(29) Schwalbe-Koda, D.; Jensen, Z.; Olivetti, E.; Gómez-Bombarelli, R. Graph Similarity Drives Zeolite Diffusionless Transformations and Intergrowth. *Nat. Mater.* **2019**, *18* (11), 1177−1181.
(30) Ruiz-Agudo, E.; Putnis, C. V.; Putnis, A. Coupled Dissolution and Precipitation at Mineral-Fluid Interfaces. In *Chem. Geol.*; Elsevier, 2014; pp 132−146. September 15..
(31) Cundy, C. S.; Cox, P. A. The Hydrothermal Synthesis of Zeolites: Precursors, Intermediates and Reaction Mechanism. *Microporous Mesoporous Mater.* **2005**, *82* (1−2), 1−78.
(32) Goel, S.; Zones, S. I.; Iglesia, E. Synthesis of Zeolites via Interzeolite Transformations without Organic Structure-Directing Agents. *Chem. Mater.* **2015**, *27* (6), 2056−2066.
(33) Muraoka, K.; Sada, Y.; Shimojima, A.; Chaikittisilp, W.; Okubo, T. Tracking the Rearrangement of Atomic Configurations during the Conversion of FAU Zeolite to CHA Zeolite. *Chem. Sci.* **2019**, *10* (37), 8533−8540.

https://doi.org/10.1021/acs.cgd.5c01166
Cryst. Growth Des. 2026, 26, 1100−1112

(34) Báfero, G. B.; Munsignatti, E. C. O.; Pastore, H. O. Lamellar-Zeolitic Transformations Mediated by Diffusionless and Recrystallization Mechanisms. *Microporous Mesoporous Mater.* **2021**, *323* (May), 111189.
(35) Su, S.; Ma, H.; Chuan, X. Hydrothermal Synthesis of Zeolite A from K-Feldspar and Its Crystallization Mechanism. *Adv. Powder Technol.* **2016**, *27* (1), 139−144.
(36) Feng, M.; Kou, Z.; Tang, C.; Shi, Z.; Tong, Y.; Zhang, K. Recent Progress in Synthesis of Zeolite from Natural Clay. In *Applied Clay Science*; Elsevier Ltd, 2023; .10.1016/j.clay.2023.107087.
(37) Xing, P.; Wang, C.; Zeng, L.; Ma, B.; Wang, L.; Chen, Y.; Yang, C. Lithium Extraction and Hydroxysodalite Zeolite Synthesis by Hydrothermal Conversion of α-Spodumene. *ACS Sustain. Chem. Eng.* **2019**, *7* (10), 9498−9505.
(38) Stepanov, A. G. Basics of Solid-State NMR for Application in Zeolite Science: Material and Reaction Characterization. In *Zeolites and Zeolite-like Materials*; Elsevier B.V., 2016; pp 137−188.
(39) Thommes, M.; Kaneko, K.; Neimark, A. V.; Olivier, J. P.; Rodriguez-Reinoso, F.; Rouquerol, J.; Sing, K. S. W. Physisorption of Gases, with Special Reference to the Evaluation of Surface Area and Pore Size Distribution (IUPAC Technical Report). *Pure Appl. Chem.* **2015**, *87* (9−10), 1051−1069.
(40) Brunauer, S.; Emmett, P. H.; Teller, E. Adsorption of Gases in Multimolecular Layers. *J. Am. Chem. Soc.* **1938**, *60* (2), 309−319.
(41) Sing, K. S. W.; Williams, R. T. Empirical Procedures for the Analysis of Physisorption Isotherms. *Adsorpt. Sci. Technol.* **2005**, *23* (10), 839−853.
(42) Kruk, M.; Jaroniec, M.; Sayari, A. Application of Large Pore MCM-41 Molecular Sieves to Improve Pore Size Analysis Using Nitrogen Adsorption Measurements. *Langmuir* **1997**, *13* (23), 6267−6273.
(43) Gurvich, L. G. Physico-Chemical Attractive Force. II. *J. Phys. Chem. Soc. Russ.* **1915**, *47*, 805.
(44) Lima, R. C.; Lopes, C. W.; Villarroel-Rocha, J.; Bieseki, L.; Sapag, K.; Pergher, S. B. C. Organic-Free Synthesis of Finned Mordenite Zeolite. *Nanomaterials* **2022**, *12* (15), 2623.
(45) Zhu, J.; Liu, Z.; Endo, A.; Yanaba, Y.; Yoshikawa, T.; Wakihara, T.; Okubo, T. Ultrafast, OSDA-Free Synthesis of Mordenite Zeolite. *CrystEngComm* **2017**, *19* (4), 632−640.
(46) Telles de Souza, J.; Ferreira Young, A.; Sousa-Aguiar, E. F.; Romano, P. N.; García-Martínez, J.; De Almeida, J. M. A. R. How Local Order Leads to Shape Selectivity in Disordered Materials: The Case of FAU-FER Interzeolite Transformation Intermediates. *ACS Catal.* **2025**, *15* (6), 4586−4595.
(47) Campos, D. O.; Monsores, A. D. F. F.; Suguihiro, N. M.; Aranda, D. A. G.; Garcia Martinez, J.; Romano, P. N.; de Almeida, J. M. A. R. Combining Mesoporosity and Shape Selectivity in FAU−MFI Interzeolite Intermediates for Renewable Xylenes Production. *ACS Sustain. Chem. Eng.* **2025**, acssuschemeng.5c05295.
(48) Mendoza-Castro, M. J.; De Oliveira-Jardim, E.; Ramírez-Marquez, N. T.; Trujillo, C. A.; Linares, N.; García-Martínez, J. Hierarchical Catalysts Prepared by Interzeolite Transformation. *J. Am. Chem. Soc.* **2022**, *144* (11), 5163−5171.
(49) Mendoza-Castro, M. J.; Qie, Z.; Fan, X.; Linares, N.; García-Martínez, J. Tunable Hybrid Zeolites Prepared by Partial Interconversion. *Nat. Commun.* **2023**, *14* (1), 1256.
(50) Koolia, F.; Li, M.; Plevertb, J. Comparative Studies on the Synthesis of Na-Magadiite, Na-Kenyaite and RUB-18 Phases. *Clay Science* **2006**, *12*, 25−30.
(51) Kwon, O.; Jeong, S.; Suh, J.; Lee, J. Hydrothermal Syntheses of Na-Magadiite and Na-Kenyaite in the Presence of Carbonate. *Bull. Korean Chem. Soc.* **1995**, 737−741.
(52) Wang, Y. R.; Wang, S. F.; Chang, L. C. Hydrothermal Synthesis of Magadiite. *Appl. Clay Sci.* **2006**, *33* (1), 73−77.
(53) Zhang, H.; Zhang, H.; Wang, P.; Zhao, Y.; Shi, Z.; Zhang, Y.; Tang, Y. Organic Template-Free Synthesis of Zeolite Mordenite Nanocrystals through Exotic Seed-Assisted Conversion. *RSC Adv.* **2016**, *6* (53), 47623−47631.
(54) Møller, K. H.; Debost, M.; Lakiss, L.; Kegnæs, S.; Mintova, S. Interzeolite Conversion of a Micronsized FAU to a Nanosized CHA Zeolite Free of Organic Structure Directing Agent with a High CO2 Capacity. *RSC Adv.* **2020**, *10* (70), 42953−42959.
(55) Chu-Jon, C.; Martinez, E.; Bertolazzo, A. A.; Banik, S.; Rimer, J. D.; Sankaranarayanan, S. K. R. S.; Molinero, V. Interzeolite Transformation through Cross-Nucleation: A Molecular Mechanism for Seed-Assisted Synthesis. *J. Am. Chem. Soc.* **2024**, *146* (48), 33204−33213.
(56) Suhendar, D.; Buchari, M. R. R.; Mukti, R. R.; Ismunandar. Simple approach in understanding interzeolite transformations using ring building units. *IOP Conf. Ser.:Mater. Sci. Eng.* **2018**, *349* (1), 012016.
(57) Marler, B.; Krysiak, Y.; Grosskreuz, I.; Gies, H.; Kolb, U. The Crystal Structure of Mineral Magadiite, Na2Si14O28(OH)2●8H2O. *Am. Mineral.* **2022**, *107* (11), 2101−2110.
(58) Tôrres, M. F.; Santos, M. F.; Silva, B. N. N.; Saqlain, M. A.; Antunes, F. P. N.; Pastore, H. O.; Leitão, A. A. Theoretical Evaluation of M/H-Magadiite and Al Modified M/H-[Al]-Magadiites Single-Atom Catalysts (M = Ag, Au, Pd, and Pt). *Surf. Sci.* **2024**, *748*, 122541.
(59) Freeman, E. E.; Neeway, J. J.; Motkuri, R. K.; Rimer, J. D.; Mpourmpakis, G. Understanding Initial Zeolite Oligomerization Steps with First Principles Calculations. *AIChE J.* **2020**, *66* (12), No. e17107.
(60) Cheng, X.; Liu, Y.; Chen, D. Mechanisms of Hydrolysis-Oligomerization of Aluminum Alkoxide Al(OC3H7)3. *J. Phys. Chem. A* **2011**, *115* (18), 4719−4728.
(61) Nienhuis, E. T.; Pouvreau, M.; Graham, T. R.; Prange, M. P.; Page, K.; Loring, J. S.; Stack, A. G.; Clark, A. E.; Schenter, G. K.; Rosso, K. M.; Pearce, C. I.; Wang, H. W. Structure and Reactivity of Sodium Aluminate Complexes in Alkaline Solutions. *J. Mol. Liq.* **2022**, *367*, 120379.
(62) Martineau, C.; Taulelle, F.; Haouas, M. The Use of 27Al NMR to Study Aluminum Compounds: A Survey of the Last 25 Years. In *PATAI'S Chemistry of Functional Groups*; John Wiley & Sons, 2016.
(63) Park, M.; Kang, Y. J.; Jang, J. H.; Seo, J. D.; Kim, J.; Paek, S. M.; Lim, W. T.; Komarneni, S. Formation Mechanism of an Al13 Keggin Cluster in Hydrated Layered Polysilicates. *Dalton Trans.* **2020**, *49* (15), 4920−4926.
(64) Pastvova, J.; Pilar, R.; Moravkova, J.; Kaucky, D.; Rathousky, J.; Sklenak, S.; Sazama, P. Tailoring the Structure and Acid Site Accessibility of Mordenite Zeolite for Hydroisomerisation of N-Hexane. *Appl. Catal., A* **2018**, *562* (January), 159−172.
(65) Brus, J.; Kobera, L.; Schoefberger, W.; Urbanová, M.; Klein, P.; Sazama, P.; Tabor, E.; Sklenak, S.; Fishchuk, A. V.; Dědeček, J. Structure of Framework Aluminum Lewis Sites and Perturbed Aluminum Atoms in Zeolites as Determined by 27Al{1H} REDOR (3Q) MAS NMR Spectroscopy and DFT/Molecular Mechanics. *Angew. Chem., Int. Ed.* **2015**, *54* (2), 541−545.
(66) Liu, Y.; Nekvasil, H.; Tossell, J. Explaining the Effects of T-O-T Bond Angles on NMR Chemical Shifts in Aluminosilicates: A Natural Bonding Orbital (NBO) and Natural Chemical Shielding (NCS) Analysis. *J. Phys. Chem. A* **2005**, *109* (13), 3060−3066.
(67) Gackowski, M.; Tarach, K.; Kuterasiński, Ł.; Podobiński, J.; Sulikowski, B.; Datka, J. Spectroscopic IR and NMR Studies of Hierarchical Zeolites Obtained by Desilication of Zeolite Y: Optimization of the Desilication Route. *Microporous Mesoporous Mater.* **2019**, *281*, 134−141.
(68) Barras, J.; Klinowski, J.; McComb, D. W. 27Al and 29Si Solid-State NMR Studies of Dealuminated Mordenite. *J. Chem. Soc., Faraday Trans.* **1994**, *90* (24), 3719−3723.
(69) Van Tendeloo, L.; Wangermez, W.; Vandekerkhove, A.; Willhammar, T.; Bals, S.; Maes, A.; Martens, J. A.; Kirschhock, C. E. A.; Breynaert, E. Postsynthetic High-Alumina Zeolite Crystal Engineering in Organic-Free Hyper-Alkaline Media. *Chem. Mater.* **2017**, *29* (2), 629−638.
(70) Robijns, S.; Devos, J.; Baeckelmans, B.; De Frene, T.; Torka Beydokhti, M.; de Oliveira-Silva, R.; De Witte, N.; Sakellariou, D.;

https://doi.org/10.1021/acs.cgd.5c01166
Cryst. Growth Des. 2026, 26, 1100−1112

Van Assche, T. R. C.; Dusselier, M. Split Syntheses: Introducing Bottom-Up Control over Aluminum in SSZ-13 and ZSM-5 Zeolites. *JACS Au* **2025**, *5* (2), 593−605.
(71) Almond, G. G.; Harris, R. K.; Franklin, K. R. A Structural Consideration of Kanemite, Octosilicate, Magadiite and Kenyaite. *J. Mater. Chem.* **1997**, *7* (4), 681−687.
(72) Kooli, F.; Kiyozumi, Y.; Mizukami, F. Novel Layered Silicate and Microporous Silica Materials in the Na-Magadiite - H2O - (TMA)2O System. *New J. Chem.* **2001**, *25* (12), 1613−1620.
(73) Pinnavaia, T. J.; Johnson, I. D.; Lipsicas, M. A 29Si MAS NMR Study of Tetrahedral Site Distributions in the Layered Silicic Acid H +-Magadiite (H2Si14O29 · NH2O) and in Na+-Magadiite (Na2Si14O29 · NH2O). *J. Solid State Chem.* **1986**, *63* (1), 118−121.
(74) Sanz-Pérez, E. S.; Fernández, A.; Arencibia, A.; Calleja, G.; Sanz, R. Hybrid Amine-Silica Materials: Determination of N Content by 29Si NMR and Application to Direct CO2 Capture from Air. *Chem. Eng. J.* **2019**, *373*, 1286−1294.
(75) Brinker, C. J.; Brow, R. K.; Tallant, D. R.; Kirkpatrick, R. J. Surface Structure and Chemistry of High Surface Area Silica Gels. *J. Non-Cryst. Solids* **1990**, *120* (1−3), 26−33.
(76) Itabashi, K.; Ikeda, T.; Matsumoto, A.; Kamioka, K.; Kato, M.; Tsutsumi, K. Syntheses and Structural Properties of Four Rb-Aluminosilicate Zeolites. *Microporous Mesoporous Mater.* **2008**, *114* (1−3), 495−506.
(77) Khodabandeh, S.; Davis, M. E. Synthesis of a Heulandite-Type Zeolite by Hydrothermal Conversion of Zeolite P1. *Chem. Commun.* **1996**, No. 10, 1205−1206.
(78) Engelhardt, G.; Fahlke, B.; Mägi, M.; Lippmaa, E. High-Resolution 29Si and 27Al NMR Studies of 29Si-Enriched ZSM-5 Zeolites. *Z. Phys. Chem.* **1985**, *266O* (1), 239−245.
(79) Fyfe, C. A.; Gobbi, G. C.; Murphy, W. J.; Ozubko, R. S.; Slack, D. A. Investigation of the Factors Affecting the 29 Si MAS NMR Linewidths of Zeolites. *Chem. Lett.* **1983**, *12* (10), 1547−1550.
(80) Pál-Borbély, G.; Auroux, A. Acidity of Isomorphically Substituted Crystalline Silicic Acids with Layer Structure. I. H-Magadiite. In *Catalysis by Microcporous Materials*; Beyer, H. K., Karge, H. G., Nagy, J. B., Kiricsi, I., Eds., 1995; Vol. *94*, pp 55−62.
(81) Lónyi, F.; Valyon, J. On the Interpretation of the NH3-TPD Patterns of H-ZSM-5 and H-Mordenite. *Microporous Mesoporous Mater.* **2001**, *47* (2−3), 293−301.
(82) Guisnet, M.; Pinard, L. Characterization of Acid-Base Catalysts through Model Reactions. *Catal. Rev. Sci. Eng.* **2018**, *60* (3), 337−436.
(83) Basu, S.; Sen, A. K. A Review on Catalytic Dehydration of Glycerol to Acetol. *ChemBioEng Rev.* **2021**, *8* (6), 633−653.
(84) Matsumura, Y.; Hashimoto, K.; Yoshida, S. Selective Dehydrogenation of Ethanol over Dehydrated Silica. *J. Chem. Soc. Chem. Commun.* **1987**, *143* (20), 1599−1600.
(85) Chandra, A. K.; Goursot, A.; Fajula, F. Proton Affinity Differences in Zeolite: A DFT Study. *J. Mol. Catal. A:Chem.* **1997**, *119* (1−3), 45−50.
(86) Kramer, G. J.; Van Santen, R. A. Theoretical Determination of Proton Affinity Differences in Zeolites. *J. Am. Chem. Soc.* **1993**, *115* (7), 2887−2897.
(87) Kim, Y. T.; Jung, K. D.; Park, E. D. A Comparative Study for Gas-Phase Dehydration of Glycerol over H-Zeolites. *Appl. Catal., A* **2011**, *393* (1−2), 275−287.
(88) Hattori, H.; Arudra, P.; Abdalla, A.; Aitani, A. M.; Al-Khattaf, S. S. Infrared Study of Silanol Groups on Dealuminated High Silica MFI Zeolite to Correlate Different Types of Silanol Groups with Activity for Conversion of 1-Butene to Propene. *Catal. Lett.* **2020**, *150* (3), 771−780.
(89) Ichihashi, H.; Ishida, M.; Shiga, A.; Kitamura, M.; Suzuki, T.; Suenobu, K.; Sugita, K. The Catalysis of Vapor-Phase Beckmann Rearrangement for the Production of ε-Caprolactam. *Catal. Surv. Asia* **2003**, *7* (4), 261−270.
(90) Rimola, A.; Costa, D.; Sodupe, M.; Lambert, J. F.; Ugliengo, P. Silica Surface Features and Their Role in the Adsorption of Biomolecules: Computational Modeling and Experiments. *Chem. Rev.* **2013**, *113*, 4216−4313.
(91) Alaithan, Z. A.; Harrison, N.; Sastre, G. Diffusivity of Propylene in One-Dimensional Medium-Pore Zeolites. *J. Phys. Chem. C* **2021**, *125* (35), 19200−19208.
(92) Cheng, Z.; Huang, S.; Li, Y.; Cai, K.; Wang, Y.; Wang, M. Y.; Lv, J.; Ma, X. Role of Bronsted Acid Sites within 8-MR of Mordenite in the Deactivation Roadmap for Dimethyl Ether Carbonylation. *ACS Catal.* **2021**, *11* (9), 5647−5657.
(93) Ferdov, S. Interzeolite Transformation from FAU-to-EDI Type of Zeolite. *Molecules* **2024**, *29* (8), 1744.
(94) Maag, A. R.; Tompsett, G. A.; Tam, J.; Ang, C. A.; Azimi, G.; Carl, A. D.; Huang, X.; Smith, L. J.; Grimm, R. L.; Bond, J. Q.; Timko, M. T. ZSM-5 Decrystallization and Dealumination in Hot Liquid Water. *Phys. Chem. Chem. Phys.* **2019**, *21* (32), 17880−17892.
(95) Huang, Y.; Jiang, Z.; Schwieger, W. Vibrational Spectroscopic Studies of Layered Silicates. *Chem. Mater.* **1999**, *11* (5), 1210−1217.
(96) Twu, J.; Dutta, P. K.; Kresge, C. T. Vibrational Spectroscopic Examination of the Formation of Mordenite Crystals. *J. Phys. Chem.* **1991**, *95* (13), 5267−5271.
(97) Pechar, F.; Rykl, D. Study of the Complex Vibrational Spectra of Natural Zeolite Mordenites. *Zeolites* **1983**, *3* (4), 329−332.
(98) Pichat, P.; Franco-Parra, C.; Barthomeuf, D. Infra-Red Structural Study of Various Type L Zeolites. *J. Chem. Soc., Faraday Trans.* **1975**, *71* (0), 991−996.
(99) Mozgawa, W. The Relation between Structure and Vibrational Spectra of Natural Zeolites. *J. Mol. Struct.* **2001**, *596* (1−3), 129−137.
(100) Flanigen, E. M.; Khatami, H.; Szymanski, H. A. Infrared Structural Studies of Zeolite Frameworks. In *Molecular Sieve zeolites-I*; American Chemical Society, 1974; pp 201−229.
(101) Kustov, L.; Borovkov, V. Y.; Kazansky, V. B. Spectra of Hydroxyl Groups in Zeolites in the Near-Infrared Region. *J. Catal.* **1981**, *72* (1), 149−159.
(102) Hanke, W.; Möller, K. Near-Infrared Study of the Dealumination and Water Desorption from Zeolites. *Zeolites* **1984**, *4* (3), 244−250.
(103) Madejová, J.; Komadel, P. Baseline Studies of the Clay Minerals Society Source Clays: Infrared Methods. *Clays Clay Miner.* **2001**, *49* (5), 410−432.
(104) Eypert-Blaison, C.; Michot, L. J.; Humbert, B.; Pelletier, M.; Villiéras, F.; Jean-Baptiste d'Espinose de la, C. Hydration Water and Swelling Behavior of Magadiite. The H+, Na+, K+, Mg2+, and Ca2+ Exchanged Forms. *J. Phys. Chem. B* **2002**, *106* (3), 730−742.
(105) Yu, Y.; Xiong, G.; Li, C.; Xiao, F. S. Characterization of Aluminosilicate Zeolites by UV Raman Spectroscopy. *Microporous Mesoporous Mater.* **2001**, *46* (1), 23−34.
(106) Król, M.; Mozgawa, W.; Barczyk, K.; Bajda, T.; Kozanecki, M. Changes in the Vibrational Spectra of Zeolites Due to Sorption of Heavy Metal Cations. *J. Appl. Spectrosc.* **2013**, *80* (5), 644−650.
(107) Annen, M. J.; Davis, M. E. Raman and 29Si MAS NMR Spectroscopy of Framework Materials Containing Three-Membered Rings. *Microporous Mater.* **1993**, *1* (1), 57−65.
(108) Kumar, M.; Li, R.; Rimer, J. D. Assembly and Evolution of Amorphous Precursors in Zeolite L Crystallization. *Chem. Mater.* **2016**, *28* (6), 1714−1727.
(109) Li, R.; Chawla, A.; Linares, N.; Sutjianto, J. G.; Chapman, K. W.; Martínez, J. G.; Rimer, J. D. Diverse Physical States of Amorphous Precursors in Zeolite Sol-Gel Syntheses. *Ind. Eng. Chem. Res.* **2018**, *57* (25), 8460−8471.
(110) Ren, N.; Subotić, B.; Bronić, J.; Tang, Y.; Dutour Sikirić, M.; Mišić, T.; Svetličić, V.; Bosnar, S.; Antonić Jelić, T. Unusual Pathway of Crystallization of Zeolite ZSM-5 in a Heterogeneous System: Phenomenology and Starting Considerations. *Chem. Mater.* **2012**, *24* (10), 1726−1737.
(111) Liebau, F.; Gies, H.; Gunawardane, R. P.; Marler, B. Classification of Tectosilicates and Systematic Nomenclature of Clathrate Type Tectosilicates: A Proposal. *Zeolites* **1986**, *6* (5), 373−377.

https://doi.org/10.1021/acs.cgd.5c01166
Cryst. Growth Des. 2026, 26, 1100−1112

(112) Qin, W.; Jain, R.; Robles Hernández, F. C.; Rimer, J. D. Organic-Free Interzeolite Transformation in the Absence of Common Building Units. *Chem.—Eur. J.* **2019**, *25* (23), 5893−5898.
(113) Dhainaut, J.; Daou, T. J.; Bidal, Y.; Bats, N.; Harbuzaru, B.; Lapisardi, G.; Chaumeil, H.; Defoin, A.; Rouleau, L.; Patarin, J. One-Pot Structural Conversion of Magadiite into MFI Zeolite Nanosheets Using Mononitrogen Surfactants as Structure and Shape-Directing Agents. *CrystEngComm* **2013**, *15* (15), 3009−3015.
(114) Cui, M.; Wang, Y.; Liu, X.; Zhu, J.; Sun, J.; Lv, N.; Meng, C. Solvothermal Conversion of Magadiite into Zeolite Omega in a Glycerol-Water System. *J. Chem. Technol. Biotechnol.* **2014**, *89* (3), 419−424.

https://doi.org/10.1021/acs.cgd.5c01166
Cryst. Growth Des. 2026, 26, 1100−1112